

# Nernst Plateau in the Quantum Limit of Low-Carrier-Density Topological Insulators

Peng-Lu Zhao,<sup>1,2,3</sup> J. L. Zhang,<sup>4,\*</sup> Hai-Zhou Lu,<sup>3,2,†</sup> and Qian Niu<sup>1,5</sup>

<sup>1</sup>Department of Physics, University of Science and Technology of China, Hefei, Anhui 230026, China

<sup>2</sup>Quantum Science Center of Guangdong-Hong Kong-Macao Greater Bay Area (Guangdong), Shenzhen 518045, China

<sup>3</sup>State Key Laboratory of Quantum Functional Materials, Department of Physics, and Guangdong Basic Research Center of Excellence for Quantum Science, Southern University of Science and Technology (SUSTech), Shenzhen 518055, China

<sup>4</sup>Anhui Province Key Laboratory of Low-Energy Quantum Materials and Devices, High Magnetic Field Laboratory, HFIPS, Chinese Academy of Sciences, Hefei 230031, China

<sup>5</sup>CAS Key Laboratory of Strongly-Coupled Quantum Matter Physics, University of Science and Technology of China, Hefei, Anhui 230026, China

Nernst effect, a transverse electric current induced by a temperature gradient, is a promising tool for revealing emergent phases of condensed matter. We find a Nernst coefficient plateau in low carrier density topological insulators, as a signature of 1D Weyl points in the quantum limit of the weak topological insulator. The plateau height is inversely proportional to the impurity density, suggesting a way to engineer infinitely large Nernst effects. The Nernst plateau also exists in strong topological insulators, at the bottom of the lowest Landau band. We show that these plateaus have been overlooked in the previous experiments and we highlight the experimental conditions to observe them. Our results may inspire more investigations of employing anomalous Nernst effect to identify emergent phases of condensed matter.

*Introduction*—Nernst effect is a thermoelectric Hall effect, exhibiting as a transverse electric current generated by a temperature gradient. It is a promising measurement method to reveal outstanding signatures than those in the conductivity. Two types of Nernst effects have been observed in the experiments [1, 2], the normal one shows a weak-field peak in metals [3–11] and superconductors [10–17] and the anomalous one shows a plateau in topological and magnetic materials in weak fields [18–28] [Fig. 1(a)]. A plateau, quantized or not, is always intriguing, thus the Nernst plateau has attracted significant attention in the past ten years. It can be explained by either the saturation of magnetization or finite Berry curvature induced by the self-rotation of Bloch wave packets [29–32]. Nevertheless, none of these mechanisms applies in strong magnetic fields, where Landau levels are formed and each level produces a quantized Hall conductivity. According to the Mott relation [33–35], both types of the Nernst effect are expected to decay and vanish in extremely strong magnetic fields.

In this Letter, however, we theoretically demonstrate that a Nernst plateau can form in the strong-field quantum limit of topological insulators [Fig. 1(b)], as the ratio of the Nernst coefficient  $S_{yx}$  to temperature  $T$

$$\frac{S_{yx}}{T} = \frac{\pi^2 k_B^2}{3e} \frac{2}{R\Gamma}, \quad (1)$$

where besides the fundamental constants (the Boltzmann constants  $k_B$ , electron charge  $e$ , and  $\pi$ ),  $R = 1$  for weak and  $R = 5$  for strong topological insulators, and the Landau-band broadening  $\Gamma$  could remain invariant in the quantum limit, as protected by a detailed charge neutrality resulted from a nontrivial topological phase transition, giving rise to the Nernst plateau. Moreover, the height of this Nernst plateau can increase infinitely with

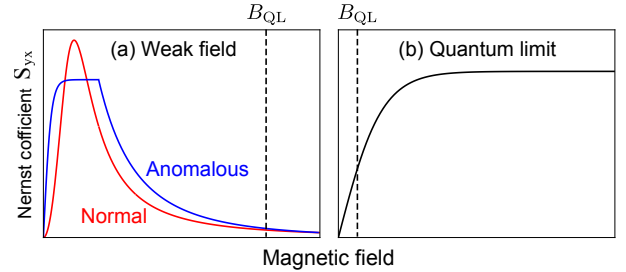


FIG. 1. (a) Schematic of the previously known two types of the Nernst effect, in terms of the dependence of the Nernst coefficient  $S_{yx}$  on the magnetic field at a fixed and low temperature  $T$ . (b) In comparison, we find a Nernst plateau beyond the expectation of the previous mechanisms, at magnetic fields far above the strong-field quantum limit  $B_{QL}$  (indicated by the black dashed lines), where only the lowest Landau band is occupied by electrons.

decreasing impurity density. Our results not only predict a Nernst plateau in the ultra-quantum limit of low-carrier-density topological insulators, but also suggest a strategy to enhance thermoelectric conversion efficiency.

*Landau bands in topological insulators*—The 3D strong and weak topological insulators can be generically described by the modified Dirac model [36],

$$H_0(\mathbf{k}) = \hbar v_x k_x \tau_z \sigma_x + \hbar v_y k_y \tau_0 \sigma_y + \hbar v_z k_z \tau_x \sigma_x + [\Delta + M_\perp (k_x^2 + k_y^2) + M_z k_z^2] \tau_0 \sigma_z, \quad (2)$$

where  $v_{x,y,z}$  are the Fermi velocities,  $\sigma$  and  $\tau$  are Pauli matrices for pseudo and real spins, respectively.  $2|\Delta|$  is the bulk gap,  $M_\perp$  and  $M_z$  are two minimal band inversion parameters used to distinguish strong and weak topological insulators [37–42]. Without loss of generality, we assume  $\Delta > 0$ , then Eq. (2) describes a strong topo-

logical insulator when  $M_z < M_\perp < 0$  [43–45], a weak topological insulator when  $M_\perp < 0$  and  $M_z > 0$ , or a normal insulator when  $M_\perp > 0$  and  $M_z > 0$  (see Sec. SI of Supplemental Material [46]).

By applying a uniform  $z$ -direction magnetic field magnetic fields  $\mathbf{B} = (0, 0, B)$ , the energy spectrum of the topological insulator turn to a series of 1D bands of Landau levels. To analyze the Landau bands (details can be found in Sec. SI of Supplemental Material [46]), the canonical wave vectors are defined by the Peierls substitution  $\mathbf{\Pi} = \mathbf{k} + e\mathbf{A}/\hbar$  with the Landau gauge potential  $\mathbf{A} = (-yB, 0, 0)$ . The ladder operators then can be constructed by  $\mathbf{\Pi}_x$  and  $\mathbf{\Pi}_y$ , which further yield the 1D Landau bands as  $E_{n\nu}^\mu(k_z) = \mu(Z - M_\perp/\ell_B^2) + \nu\sqrt{(M_z k_z^2 + 2M_\perp n/\ell_B^2 + \Delta)^2 + (\sqrt{2n}\hbar v_\perp/\ell_B)^2}$  for  $n \geq 1$  and  $E_{0\nu}(k_z) = \nu|M_z k_z^2 + M_\perp/\ell_B^2 + \Delta - Z|$  for the Lowest Landau bands. Here,  $\mu$  and  $\nu$  take values of  $\pm$ ,  $v_\perp = \sqrt{v_x v_y}$ ,  $\ell_B = \sqrt{\hbar/eB}$ , and  $Z = g\mu_B B/2$ , where  $g$  represents the g-factor and  $\mu_B$  stands for the Bohr magneton.  $Z$  represents the Zeeman energy, as we have included a Zeeman coupling term  $H_Z = -g\mu_B B\tau_z\sigma_0/2$  in the free Hamiltonian. The normalized eigenvectors of all Landau bands can be found and are uniformly denoted as  $|n\mathbf{k}, +(\nu), +(\mu)\rangle$ .

*Conductivities and Nernst coefficient*—In the strong-field quantum limit where only the lowest Landau bands cross the Fermi energy, the Nernst coefficient can be found according to the Mott relation, which reads

$$S_{xy} = \frac{\pi^2 k_B^2 T}{3e} \frac{\partial \Theta_H}{\partial E_F}, \quad (3)$$

where the Hall angle  $\Theta_H \equiv \arctan(\sigma_{xy}/\sigma_{xx})$ , the longitudinal and Hall conductivities are found by the Kubo-Středa formula [47] at low temperature and in the quantum limit (Sec. SIII of Supplemental Material [46]) as

$$\sigma_{xx} = \frac{\hbar v_\perp^2 e^2}{2\pi^2 \ell_B^2} \int \frac{dk_z}{2\pi} \sum_{\mu, \nu = \pm} \mathcal{A}_{0\mu} \mathcal{T}_\mu^\nu \mathcal{A}_{1\nu}, \quad (4)$$

$$\sigma_{xy} = \frac{\hbar v_\perp^2 e^2}{2\pi^2 \ell_B^2} \int \frac{dk_z}{2\pi} \sum_{\mu, \mu' = \pm} \mathcal{T}_\mu^\nu (\mathcal{A}_{0\mu} \mathcal{G}_{1\nu} - \mathcal{G}_{0\mu} \mathcal{A}_{1\nu}), \quad (5)$$

where  $\mathcal{A}_{0\mu} = \Gamma/[(E_{0\mu} - E_F)^2 + \Gamma^2]$  and  $\mathcal{A}_{1\nu} = \Gamma/[(E_{1\nu}^\mu - E_F)^2 + \Gamma^2]$  represent the spectral functions for the  $E_{0\mu}$  and  $E_{1\nu}^\mu$  ( $\mu = -\nu$ ) bands, respectively, and  $\mathcal{T}_\mu^\nu$  denotes the transition probability between these two bands. Here,  $\mathcal{T}_\mu^\nu(\mu\nu = +) = [\sin(\theta/2) + \gamma \cos(\theta/2)]^2$  and  $\mathcal{T}_\mu^\nu(\mu\nu = -) = [\cos(\theta/2) - \gamma \sin(\theta/2)]^2$ , where  $\gamma = \sqrt{2}M_\perp/(\hbar v_\perp \ell_B)$  is a dimensionless parameter, and for  $\theta \in (0, \pi)$ ,  $\cos \theta = E_d/\sqrt{E_d^2 + (\sqrt{2}\hbar v_\perp/\ell_B)^2}$  with  $E_d = M_z k_z^2 + 2M_\perp/\ell_B^2 + \Delta$ .  $\mathcal{G}_{0\mu} = [(E_{0\mu} - E_F)^2 - \Gamma^2]/[(E_{0\mu} - E_F)^2 + \Gamma^2]^2$  and  $\mathcal{G}_{1\nu} = [(E_{1\nu}^\mu - E_F)^2 - \Gamma^2]/[(E_{1\nu}^\mu - E_F)^2 + \Gamma^2]^2$ . Equations (4) and (5) are derived under  $k_B T \ll \Gamma$  to ensure the Mott relation holds.

High temperatures and inelastic electron-phonon scattering can break the Mott relation [33–35]. For  $k_B T \ll \Gamma$ , phonons are frozen out, inelastic scattering is negligible, and the Mott relation remains valid. Additionally, the quantum limit approximation is well justified when the broadening is much smaller than the Landau band spacing at  $k_z = 0$ , which for typical topological insulators [37, 48, 49] is expressed as  $\Gamma \ll \sqrt{2}\hbar v_\perp/\ell_B$ .

*Nernst plateau in weak topological insulators*—By substituting the calculated conductivities (Eq. (4) and Eq. (5)) into the Mott relation (Eq. (3)), one can obtain the evolution of  $S_{xy}$  with respect to  $B$ . For weak topological insulators, we found that  $S_{xy}$  forms a field-independent plateau after a critical value ( $\gg B_{QL}$ ) (see Fig. 2(b)). This behavior manifests under the stringent condition of an extremely low carrier density.

For a detailed explanation of our findings, we begin by illustrating the evolution of the lowest Landau band with  $B$ . As shown in Fig. 3(a), the two lowest Landau bands have a gap at the quantum limit for a weak topological insulator ( $M_\perp, M_z > 0$ , and  $\Delta > 0$ ). As  $B$  increases, the  $E_{0+}$  band shifts downwards while the  $E_{0-}$  band shifts upwards. Consequently, the gap between them decreases and closes at  $B_1 = \Delta/(-M_\perp e/\hbar + g\mu_B/2)$  (see Fig. 3(b)). As  $B$  increases further to  $B_2$  (see Supplemental Material, Sec. SV [46] for the calculation of  $B_2$ ), which is determined by the real root of

$$(g\mu_B - 2M_\perp e/\hbar) B_2^3 - 2\Delta B_2^2 - M_z (\pi\hbar n_0/e)^2 = 0, \quad (6)$$

the  $E_{0-}$  band reaches the Fermi energy. Here, the carrier density is given by  $n_0 = \int dk_z \sum_{n,\mu} [f(E_{n+}^\mu) - (1 - f(E_{n-}^\mu))]/4\pi^2 \ell_B^2$ . Consequently, the Fermi surface in  $k_z$ -space undergoes a transition from two points to three points, marking a Lifshitz transition [50–52], which is depicted in Fig. 3(c). Figure 3(d) illustrates that with further increase in  $B$ , the Fermi energy approaches the Weyl points, forming an ideal 1D Weyl state. Our calculations suggest that such an ideal 1D Weyl state gives rise to the flat  $S_{xy}$ .

To calculate  $S_{xy}(B)$ , we need to know how  $E_F$  changes with  $B$ . Typically, this can be done by keeping either  $E_F$  or the carrier density  $n_0$  constant [53, 54]. When assuming  $n_0$  is constant, as shown in Fig. 2(a), the calculated  $E_F$  decreases with increasing  $B$  before the Lifshitz transition, after which  $E_F$  becomes almost field-independent. Therefore,  $S_{xy}$  is calculated by keeping  $n_0$  constant before the Lifshitz transition and  $E_F$  constant after the transition. The results of  $S_{xy}(B)$  at  $T = 2$  K are plotted in Fig. 2(b), showing that  $S_{xy}$  rapidly decays with increasing  $B$  before the Lifshitz transition. After the transition,  $S_{xy}$  quickly saturates, forming a field-independent plateau. Such a plateau can be analytically obtained as a result of the ideal 1D Weyl state shown in Fig. 3(d). Due to charge neutrality at the Weyl point,  $\sigma_{xy} = 0$ , and

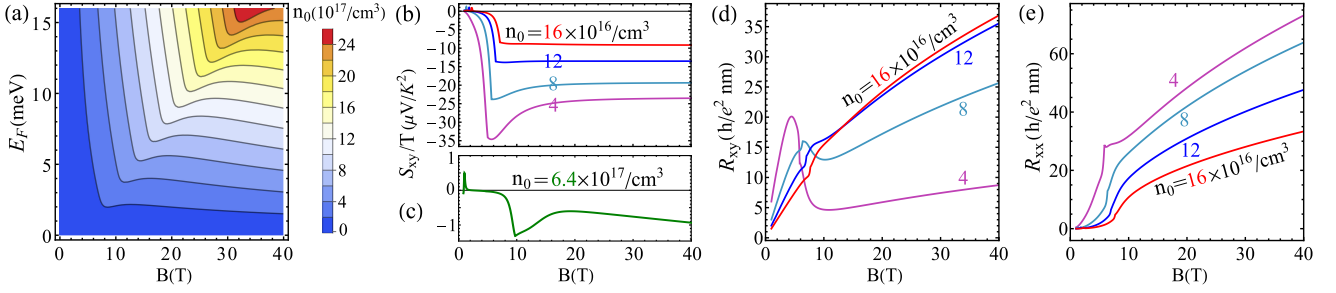


FIG. 2. Computed functions of  $E_F(B)$ ,  $S_{xy}(B)$ ,  $R_{xy}(B)$ , and  $R_{xx}(B)$  for weak topological insulators at  $T = 2$  K. (a) Contour plot in the  $B - E_F$  plane for a fixed carrier density  $n_0$  of weak topological insulators. Each line represents a constant  $n_0$ , and the different colors correspond to varying values of  $n_0$ , which are labeled in the right panel. (b), (d), and (e) Calculated  $S_{xy}(B)$ ,  $R_{xy}(B)$ , and  $R_{xx}(B)$ , respectively, for different carrier densities labelled by the colored numbers. All plots begin at  $B = 1$  T—at the quantum limit for  $n_0 = 4 \times 10^{16}/\text{cm}^3$ , but at the second Landau band for the other three carrier densities. (c) Calculated  $S_{xy}(B)$  with an  $n_0$  higher than those in (b); in this case,  $S_{xy}$  does not exhibit a plateau as in (b). This plot begins in the second Landau band at 6 T. In all diagrams, we take  $M_{\perp} = -12 \text{ eV} \cdot \text{\AA}^2$ ,  $M_z = 3 \text{ eV} \cdot \text{\AA}^2$ ,  $\Delta = 2.5 \text{ meV}$ ,  $v_{\perp} = 5 \times 10^3 \text{ m/s}$ ,  $g = 12$ , and  $\Gamma = 2 \text{ meV}$ . The quantum limits for  $n_0 = (4, 8, 12, 16, 64) \times 10^{16}/\text{cm}^3$  are  $B_0 = 0.77, 1.32, 1.82, 2.28, \text{ and } 6.81 \text{ T}$ , respectively.

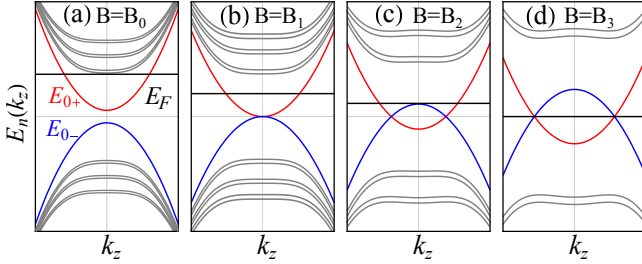


FIG. 3. Evolution of Landau bands with increasing  $B$  at several critical values. The red, blue and gray lines are for the 0th Landau bands  $E_{0+}$ ,  $E_{0-}$  and high-index Landau bands, respectively. The black line represents the Fermi energy  $E_F$ . (a) The quantum limit reaches at  $B_0$ , where the Fermi energy touches the band bottom of  $E_{1+}$ . (b) The gap of the 0th Landau band closes at  $B_1$ . (c) The Lifshitz transition happens at  $B_2$ , where  $E_F$  crosses the bottom of  $E_{0-}$ . (d) Ideal 1D Weyl states emerge at  $B_3$ , with all Weyl points located at  $E_F$ .

as a result,

$$S_{xy} = \pi^2 k_B^2 T / 3e \sigma_{xx}^{-1} \partial \sigma_{xy} / \partial E_F. \quad (7)$$

Moreover, Eq. (4) and Eq. (5) in an ideal Weyl state produce (see Supplemental Material, Sec. SVIA[46])

$$\sigma_{xx} = \frac{e^2}{\pi h} \frac{\Gamma}{2M_z k_w}, \quad \frac{\partial \sigma_{xy}}{\partial E_F} = -\frac{e^2}{\pi h} \frac{1}{M_z k_w}, \quad (8)$$

where  $k_w = \sqrt{[(-M_{\perp} e / \hbar + g \mu_B / 2) B - \Delta] / M_z}$  representing the position of the Weyl point. Substituting Eq. (8) into Eq. (7) yields  $S_{xy} / T = -2\pi^2 k_B^2 / (3e\Gamma)$ , which corresponds to  $R = 1$  in Eq. (1). Additionally, as shown in Supplemental Material Sec. SVIC [46], each subfigure in Fig. 3 leads to a special point in the Nernst coefficient curve shown in Fig. 2(b). Specifically, Fig. 3(a) leads to the peak value of the Nernst coefficient in Fig. 2(b); Fig. 3(b) leads to the point where the Nernst coefficient

crosses zero in Fig. 2(b); and Fig. 3(c) leads to the valley value in Fig. 2(b).

The emergence of this plateau is highly sensitive to the carrier density  $n_0$ . As shown in Fig. 2(c), when  $n_0$  is increased to be  $6.4 \times 10^{17}/\text{cm}^3$ , no plateau appears regardless of the magnitude of  $B$ . The main reason is that for such an  $n_0$ , the  $E_F$  after the Lifshitz transition is relatively high (see Fig. 2(a)), thus far from the ideal Weyl state. For such case, we have also obtained approximate result of  $S_{xy}/T$  under strong magnetic field (see Supplemental Material, Sec. SVI [46]), which clearly demonstrates the dependence of  $S_{xy}$  on  $B$  and shows that  $S_{xy}$  does not exhibit a plateau in strong magnetic fields. Furthermore, Eq. (6) shows that  $B_2 \propto n_0^{2/3}$ , and Fig. 2(a) show that as  $n_0$  decreases, the Fermi energy at  $B_2$  is closer to the 1D Weyl point, meaning  $B_3$  decreases with  $n_0$ . Therefore, the emergence of a Nernst plateau within experimentally accessible fields requires  $n_0$  to be sufficiently low—a condition independent of specific material details—making our prediction highly universal.

The experimental phenomenon of the Nernst plateau bears resemblance to that of the anomalous Nernst effect. To distinguish between them, we also computed the behaviors of the corresponding  $R_{xy}(B)$  and  $R_{xx}(B)$ . Figure 2(d) illustrates the variation of  $R_{xy}$  with  $B$ , showing that  $R_{xy}$  does not exhibit a plateau. This is a significant distinction between our results and the experimental phenomenon of anomalous Nernst effect, as the plateau in anomalous Nernst effect typically accompanies the anomalous Hall plateau [2, 20, 55]. Furthermore, Eq. (8) indicates that when the  $S_{xy}$  plateau appears,  $R_{xx}$  increases with  $B$  according to  $\sqrt{(-M_{\perp} e / \hbar + g \mu_B / 2) B - \Delta}$ , as shown in Fig. 2(e). Observing such behaviors of  $R_{xx}$  in experiments provides additional support for validating our plateau theory.

*Nernst plateau in strong topological insulators*—We will

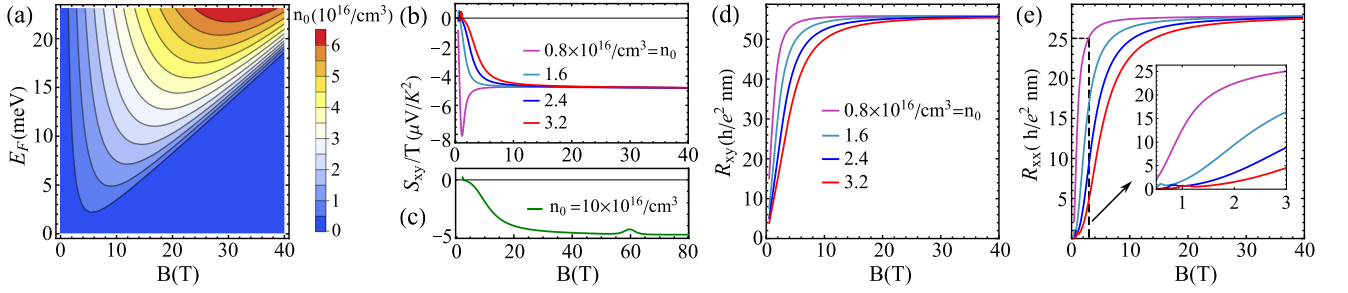


FIG. 4. Computed functions of  $E_F(B)$ ,  $S_{xy}(B)$ ,  $R_{yx}(B)$ , and  $R_{xx}(B)$  for strong topological insulators at  $T = 2$  K. (a) Contour plot in the  $B - E_F$  plane for a fixed carrier density  $n_0$  of strong topological insulators. (b), (d), and (e) Calculated  $S_{xy}(B)$ ,  $R_{yx}(B)$ , and  $R_{xx}(B)$ , respectively, for different carrier densities labelled by the colored numbers. All plots begin at  $B = 0.5\Gamma$ —at the quantum limit for  $n_0 = 0.8 \times 10^{16}/\text{cm}^3$ , but at the second Landau band for the other three carrier densities. The inset in (e) plotted  $R_{xx}(B)$  for  $B \in (0.5, 3)\text{T}$ , and the labels for the lines in (e) are the same as those in (d). (c) Calculated  $S_{xy}(B)$  with an  $n_0$  higher than those in (b); in this case,  $S_{xy}$  is not flat even for  $B \sim 100\text{T}$ . This plot begins in the second Landau band at  $3\text{T}$ . For all diagrams, we take  $M_{\perp} = -120\text{eV} \cdot \text{\AA}^2$ ,  $M_z = -12\text{eV} \cdot \text{\AA}^2$ . The values of  $\Delta$ ,  $v_{\perp}$ ,  $g$ , and  $\Gamma$  are the same as those used in Fig. 2. The quantum limits for  $n = (0.8, 1.6, 2.4, 3.2, 10) \times 10^{16}/\text{cm}^3$  are  $B_0 = 0.34, 0.61, 0.86, 1.11$ , and  $3.11\text{T}$ , respectively.

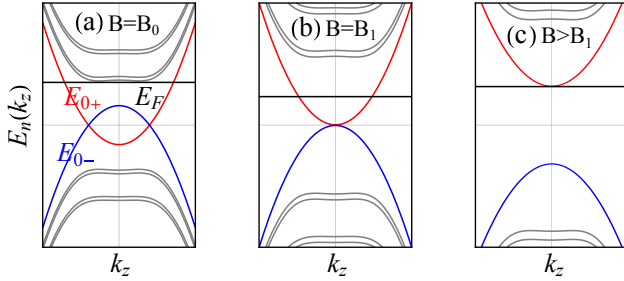


FIG. 5. Evolution of Landau bands for a strong topological insulator under selected magnetic fields. The labels of the lines are the same as those in Fig. 3. (a) The quantum limit reaches at  $B_0$ . (b) Two Weyl points merge into one at  $B_1$ . (c) The gap between two 0th Landau bands opens after  $B_1$ , and as  $B$  increases,  $E_F$  gradually pushes to the band bottom.

demonstrate that the flat Nernst effect obtained in weak topological insulators also emerges in strong topological insulators (see Fig. 4(b)), albeit requiring lower carrier concentrations and involving distinct mechanisms. Firstly, as shown in Fig. 5, the evolution of Landau bands in strong topological insulators behaves exactly opposite to that depicted in Fig. 3 for weak topological insulators. For strong topological insulators ( $M_z < M_{\perp} < 0$ , and  $\Delta > 0$ ), the Weyl points formed by  $E_{0+}$  and  $E_{0-}$  are present in weak magnetic fields (see Fig. 5(a)). As  $B$  increases,  $E_{0+}$  moves upward, and  $E_{0-}$  moves downward. When reaching  $B_1$ , the two Weyl points merge into one, as shown in Fig. 5(b). Figure Fig. 5(c) illustrates that with a further increase in  $B$ , a gap of size  $2(-M_{\perp}e/\hbar + g\mu_B/2)(B - B_1)$  opens between the two 0th Landau bands.

When calculating  $S_{xy}(B)$  for strong topological insulators, we always keep the carrier density  $n_0$  constant. If we keep  $E_F$  constant, the system will quickly become in-

ulating with increasing  $B$  because the  $E_{0+}$  band moves upward and the  $E_{0-}$  band moves downward. With  $n_0$  being constant, as shown in Fig. 4(a), the calculated  $E_F(B)$  first decreases and then increases almost linearly as  $B$  increases. Using the calculated  $E_F(B)$  to compute the  $S_{xy}(B)$  yields the results shown in Fig. 4(b). Clearly,  $S_{xy}(B)$  also flattens in strong magnetic fields. Compared to the case of weak topological insulators shown in Fig. 2(b), the carrier density here is nearly an order of magnitude lower, and while the Nernst plateau values vary with carrier density in weak topological insulators, they remain constant in this case. The flat  $S_{xy}$  appeared here can be understood as the effect of the band bottom shown in Fig. 5(c), which is completely different from the ideal Weyl state in the case of weak topological insulators. Near the band bottom,  $\sigma_{xy}$  is comparable to  $\sigma_{xx}$ . To obtain the approximate results of the Nernst coefficient, we need to calculate the asymptotic results of  $\sigma_{xy}$ ,  $\sigma_{xx}$ ,  $\partial\sigma_{xy}/\partial E_F$  and  $\partial\sigma_{xx}/\partial E_F$  separately. The detailed calculations are presented in Supplemental Material, Sec. SVIB [46], and the approximate results are as follows:

$$\sigma_{xx} = \frac{e^2}{\pi\hbar} \frac{\sqrt{\Gamma}}{4\sqrt{2}|M_z|}, \quad \frac{\partial\sigma_{xx}}{\partial E_F} = \frac{e^2}{\pi\hbar} \frac{1}{8\sqrt{2}|M_z|\Gamma}, \quad (9)$$

$$\sigma_{xy} = -\frac{e^2}{\pi\hbar} \frac{\sqrt{\Gamma}}{2\sqrt{2}|M_z|}, \quad \frac{\partial\sigma_{xy}}{\partial E_F} = -\frac{e^2}{\pi\hbar} \frac{3}{4\sqrt{2}|M_z|\Gamma}. \quad (10)$$

The asymptotic value of the Nernst coefficient is  $S_{xy}/T = -2\pi^2 k_B^2 / (15e\Gamma)$ , i.e., the result for  $R = 5$  in Eq. (1), which exactly gives the value of the plateau in Fig. 4(b) when  $\Gamma = 2\text{meV}$ . Experimentally observing the plateau requires a low density. As shown in Fig. 4(c), when  $n = 6.4 \times 10^{16}/\text{cm}^3$ , no plateau appears even at magnetic fields as high as  $80\text{T}$ , a value exceeds the limit of steady magnetic fields achievable in current experiments.

To distinguish the flat Nernst effect in strong topo-

logical insulators from the case in weak topological insulators and the anomalous Nernst behavior, we calculated  $R_{xy}(B)$  and  $R_{xx}(B)$ , which are shown in Fig. 4(d) and Fig. 4(e), respectively. Clearly,  $R_{xy}(B)$  and  $R_{xx}(B)$  also become flat under strong magnetic fields, and the values of the plateaus can be obtained through  $\sigma_{xx}$  and  $\sigma_{xy}$  in Eq. (9) and Eq. (10), respectively. Simultaneous saturation of  $R_{xy}(B)$  and  $R_{xx}(B)$  is rare in topological insulators but was recently observed in ZrTe<sub>5</sub> [56, 57].

*Experimental Observations*—So far, only a few experiments have observed the Nernst plateau in the quantum limit. Recent experiments in HfTe<sub>5</sub> [58] have observed Nernst plateaus in magnetic fields ranging from 15T to 32T ( $B_{QL} \sim 1.5T$ ), and the measured  $R_{xx}$  fits well with  $\sqrt{B}$  when the Nernst plateau appears. Given that recent infrared magneto-optical experiments have identified HfTe<sub>5</sub> as a weak topological insulator [42], and that our model Eq. (2) and the parameters in Fig. 2 also apply to HfTe<sub>5</sub>, we believe that the experimental results in [58] support our Nernst plateau theory for weak topological insulators. For the case of strong topological insulators, we think that the Nernst plateau observed earlier in ZrTe<sub>5</sub> [59] can be explained by our theory. First, our model Eq. (2) and the parameters in Fig. 4 apply to ZrTe<sub>5</sub> [38, 60]. Second, the carrier density (hole) is very low, leading to  $B_{QL} \sim 0.3T$  [59, 61, 62], while the observed Nernst plateau appears in the 3–6T range, which is well beyond the quantum limit.

We anticipate that more experiments reporting this phenomenon in other typical topological insulators such as Bi<sub>2</sub>Se<sub>3</sub>, Bi<sub>2</sub>Te<sub>3</sub>, and Sb<sub>2</sub>Te<sub>3</sub> [37, 48, 49]. For these materials, the Hamiltonian includes an additional term,  $(C + D_z k_z^2 + D_\perp k_\perp^2)I_{4 \times 4}$ . This term breaks the electron-hole symmetry, resulting in different masses for the lowest electron and hole Landau bands, but does not affect the existence of the Nernst plateau given by Eq. (1) (see Supplemental Material, Sec. SVIII [46]). However, the challenge in observing the Nernst plateau in these materials is engineering a sufficiently low  $n_0$ .

*Discussion*—In our calculations, we assumed  $\Gamma$  to be field-independent, as supported by previous studies [63–66]. Since the Nernst plateau value is proportional to  $1/\Gamma$ , we confirmed  $\Gamma$  remains field-independent by calculating it using the Born approximation with Gaussian disorder [67–70]. Details are in the Supplemental Material, Sec. SVII [46]. The results show that both strong and weak topological insulators can have a field-independent  $\Gamma$  when the Nernst plateau appears. The Nernst plateau value is approximately inversely proportional to impurity density. Reducing the impurity density allows the Nernst plateau value predicted by our theory to surpass the current record, albeit constrained by an upper limit (see Supplemental Material, Sec. SVIIC [46]), thereby significantly improving thermoelectric conversion efficiency.

*Acknowledgments*—We thank Yang Gao, Jian-hui Zhou, Zhi Wang and Song-bo Zhang for fruitful discussions.

The work is supported by the National Key R&D Program of China (Grants No. 2023YFA1406300, No. 2022YFA1403700 and No. 2022YFA1602602), the National Natural Science Foundation of China (Grants No. 12304074, No. 12234017, No. 12374041, No.12525401, No.12474053, and No. 12350402), Guangdong Basic and Applied Basic Research Foundation (Grant No. 2023B0303000011), Guangdong Provincial Quantum Science Strategic Initiative (Grants No. GDZX2201001 and No. GDZX2401001), the Science, Technology and Innovation Commission of Shenzhen Municipality (Grant No.ZDSYS20190902092905285), High-level Special Funds (Grant No. G03050K004), the New Cornerstone Science Foundation through the XPLOER PRIZE, and the Basic Research Program of the Chinese Academy of Sciences Based on Major Scientific Infrastructures (Grant No. JZHKYPT-2021-08). The numerical calculations were supported by the Center for Computational Science and Engineering of SUSTech.

*Data availability*—No data were created or analyzed in this article.

---

\* zhangjinglei@hmf.ac.cn

† luhz@sustech.edu.cn

- [1] K. Behnia, The Nernst effect and the boundaries of the Fermi liquid picture, *J. Phys.: Condens. Matter* **21**, 113101 (2009).
- [2] K. Behnia and H. Aubin, Nernst effect in metals and superconductors: a review of concepts and experiments, *Rep. Prog. Phys.* **79**, 046502 (2016).
- [3] J. H. Mangez, J. P. Issi, and J. Heremans, Transport properties of bismuth in quantizing magnetic fields, *Phys. Rev. B* **14**, 4381 (1976).
- [4] P. Li and R. L. Greene, Normal-state Nernst effect in electron-doped Pr<sub>2-x</sub>Ce<sub>x</sub>CuO<sub>4- $\delta$</sub> : Superconducting fluctuations and two-band transport, *Phys. Rev. B* **76**, 174512 (2007).
- [5] R. Bel, K. Behnia, and H. Berger, Ambipolar Nernst Effect in NbSe<sub>2</sub>, *Phys. Rev. Lett.* **91**, 066602 (2003).
- [6] E. S. Choi, J. S. Brooks, H. Kang, Y. J. Jo, and W. Kang, Resonant Nernst Effect in the Metallic and Field-Induced Spin Density Wave States of (TMTSF)<sub>2</sub>ClO<sub>4</sub>, *Phys. Rev. Lett.* **95**, 187001 (2005).
- [7] A. Pourret, K. Behnia, D. Kikuchi, Y. Aoki, H. Sugawara, and H. Sato, Drastic Change in Transport of Entropy with Quadrupolar Ordering in PrFe<sub>4</sub>P<sub>12</sub>, *Phys. Rev. Lett.* **96**, 176402 (2006).
- [8] Y. Kasahara, T. Iwasawa, H. Shishido, T. Shibauchi, K. Behnia, Y. Haga, T. D. Matsuda, Y. Onuki, M. Sigrist, and Y. Matsuda, Exotic Superconducting Properties in the Electron-Hole-Compensated Heavy-Fermion “Semimetal” URu<sub>2</sub>Si<sub>2</sub>, *Phys. Rev. Lett.* **99**, 116402 (2007).
- [9] K. Behnia, M.-A. Méasson, and Y. Kopelevich, Nernst Effect in Semimetals: The Effective Mass and the Figure of Merit, *Phys. Rev. Lett.* **98**, 076603 (2007).
- [10] P. Spathis, H. Aubin, A. Pourret, and K. Behnia, Nernst

- effect in the phase-fluctuating superconductor  $\text{InO}_x$ , *Europhysics Letters* **83**, 57005 (2008).
- [11] A. Pourret, H. Aubin, J. Lesueur, C. A. Marrache-Kikuchi, L. Bergé, L. Dumoulin, and K. Behnia, Length scale for the superconducting Nernst signal above  $T_c$  in  $\text{Nb}_{0.15}\text{Si}_{0.85}$ , *Phys. Rev. B* **76**, 214504 (2007).
- [12] R. P. Huebener and A. Seher, Nernst Effect and Flux Flow in Superconductors. II. Lead Films, *Phys. Rev.* **181**, 710 (1969).
- [13] A. Pourret, H. Aubin, J. Lesueur, C. A. Marrache-Kikuchi, L. Bergé, L. Dumoulin, and K. Behnia, Observation of the Nernst signal generated by fluctuating Cooper pairs, *Nat. Phys.* **2**, 683 (2006).
- [14] F. F. Tafti, F. Laliberté, M. Dion, J. Gaudet, P. Fournier, and L. Taillefer, Nernst effect in the electron-doped cuprate superconductor  $\text{Pr}_{2-x}\text{Ce}_x\text{CuO}_4$ : Superconducting fluctuations, upper critical field  $H_{c2}$ , and the origin of the  $T_c$  dome, *Phys. Rev. B* **90**, 024519 (2014).
- [15] J. Chang, N. Doiron-Leyraud, O. Cyr-Choinière, G. Grissonnanche, F. Laliberté, E. Hassinger, J.-P. Reid, R. Daou, S. Pyon, T. Takayama, H. Takagi, and L. Taillefer, Decrease of upper critical field with underdoping in cuprate superconductors, *Nat. Phys.* **8**, 751 (2012).
- [16] Z. A. Xu, N. P. Ong, Y. Wang, T. Kakeshita, and S. Uchida, Vortex-like excitations and the onset of superconducting phase fluctuation in underdoped  $\text{La}_{2-x}\text{Sr}_x\text{CuO}_4$ , *Nature* **406**, 486 (2000).
- [17] Y. Wang, L. Li, and N. P. Ong, Nernst effect in high- $T_c$  superconductors, *Phys. Rev. B* **73**, 024510 (2006).
- [18] W. L. Lee, S. Watauchi, V. L. Miller, R. J. Cava, and N. P. Ong, Anomalous Hall heat current and Nernst effect in the  $\text{CuCr}_2\text{Se}_{4-x}\text{Br}_x$  ferromagnet, *Phys. Rev. Lett.* **93**, 226601 (2004).
- [19] T. Miyasato, N. Abe, T. Fujii, A. Asamitsu, S. Onoda, Y. Onose, N. Nagaosa, and Y. Tokura, Crossover Behavior of the Anomalous Hall Effect and Anomalous Nernst Effect in Itinerant Ferromagnets, *Phys. Rev. Lett.* **99**, 086602 (2007).
- [20] Y. Pu, D. Chiba, F. Matsukura, H. Ohno, and J. Shi, Mott Relation for Anomalous Hall and Nernst Effects in  $\text{Ga}_{1-x}\text{Mn}_x\text{As}$  Ferromagnetic Semiconductors, *Phys. Rev. Lett.* **101**, 117208 (2008).
- [21] M. Ikhlas, T. Tomita, T. Koretsune, M. T. Suzuki, D. Nishio-Hamane, R. Arita, Y. Otani, and S. Nakatsuji, Large anomalous Nernst effect at room temperature in a chiral antiferromagnet, *Nat. Phys.* **13**, 1085 (2017).
- [22] X. Li, L. Xu, L. Ding, J. Wang, M. Shen, X. Lu, Z. Zhu, and K. Behnia, Anomalous Nernst and Righi-Leduc Effects in  $\text{Mn}_3\text{Sn}$ : Berry Curvature and Entropy Flow, *Phys. Rev. Lett.* **119**, 056601 (2017).
- [23] X. Li, L. Xu, H. Zuo, A. Subedi, Z. Zhu, and K. Behnia, Momentum-space and real-space Berry curvatures in  $\text{Mn}_3\text{Sn}$ , *SciPos Phys.* **5**, 063 (2018).
- [24] A. Sakai, Y. P. Mizuta, A. A. Nugroho, R. Sihombing, T. Koretsune, M. T. Suzuki, N. Takemori, R. Ishii, D. Nishio-Hamane, R. Arita, P. Goswami, and S. Nakatsuji, Giant anomalous Nernst effect and quantum-critical scaling in a ferromagnetic semimetal, *Nat. Phys.* **14**, 1119 (2018).
- [25] S. N. Guin, P. Vir, Y. Zhang, N. Kumar, S. J. Watzman, C. Fu, E. Liu, K. Manna, W. Schnelle, J. Gooth, C. Shekhar, Y. Sun, and C. Felser, Zero-Field Nernst Effect in a Ferromagnetic Kagome-Lattice Weyl-Semimetal  $\text{Co}_3\text{Sn}_2\text{S}_2$ , *Adv. Mater.* **31**, 1806622 (2019).
- [26] L. Xu, X. Li, X. Lu, C. Collignon, H. Fu, J. Koo, B. Fauqué, B. Yan, Z. Zhu, and K. Behnia, Finite-temperature violation of the anomalous transverse wiedemann-franz law, *Sci. Adv.* **6**, eaaz3522 (2020).
- [27] H. Yang, W. You, J. Wang, J. Huang, C. Xi, X. Xu, C. Cao, M. Tian, Z. A. Xu, J. Dai, and Y. Li, Giant anomalous Nernst effect in the magnetic Weyl semimetal  $\text{Co}_3\text{Sn}_2\text{S}_2$ , *Phys. Rev. Mater.* **4**, 024202 (2020).
- [28] C. Wuttke, F. Caglieris, S. Sykora, F. Scaravaggi, A. U. Wolter, K. Manna, V. Süß, C. Shekhar, C. Felser, B. Büchner, and C. Hess, Berry curvature unravelled by the anomalous Nernst effect in  $\text{Mn}_3\text{Ge}$ , *Phys. Rev. B* **100**, 085111 (2019).
- [29] M.-C. Chang and Q. Niu, Berry Phase, Hyperorbits, and the Hofstadter Spectrum, *Phys. Rev. Lett.* **75**, 1348 (1995).
- [30] M.-C. Chang and Q. Niu, Berry phase, hyperorbits, and the Hofstadter spectrum: Semiclassical dynamics in magnetic Bloch bands, *Phys. Rev. B* **53**, 7010 (1996).
- [31] G. Sundaram and Q. Niu, Wave-packet dynamics in slowly perturbed crystals: Gradient corrections and Berry-phase effects, *Phys. Rev. B* **59**, 14915 (1999).
- [32] D. Xiao, M. C. Chang, and Q. Niu, Berry phase effects on electronic properties, *Rev. Mod. Phys.* **82**, 1959 (2010).
- [33] L. Smrčka and P. Středa, Transport coefficients in strong magnetic fields, *J. Phys. C: Solid State Phys.* **10**, 2153 (1977).
- [34] M. Jonson and G. D. Mahan, Mott's formula for the thermopower and the Wiedemann-Franz law, *Phys. Rev. B* **21**, 4223 (1980).
- [35] M. Jonson and S. M. Girvin, Thermoelectric effect in a weakly disordered inversion layer subject to a quantizing magnetic field, *Phys. Rev. B* **29**, 1939 (1984).
- [36] S.-Q. Shen, *Topological Insulators*, 2nd ed. (Springer-Verlag, Berlin Heidelberg, 2017).
- [37] H. Zhang, C.-X. Liu, X.-L. Qi, X. Dai, Z. Fang, and S.-C. Zhang, Topological insulators in  $\text{Bi}_2\text{Se}_3$ ,  $\text{Bi}_2\text{Te}_3$  and  $\text{Sb}_2\text{Te}_3$  with a single Dirac cone on the surface, *Nat. Phys.* **5**, 438 (2009).
- [38] R. Y. Chen, Z. G. Chen, X.-Y. Song, J. A. Schneeloch, G. D. Gu, F. Wang, and N. L. Wang, Magnetoinfrared Spectroscopy of Landau Levels and Zeeman Splitting of Three-Dimensional Massless Dirac Fermions in  $\text{ZrTe}_5$ , *Phys. Rev. Lett.* **115**, 176404 (2015).
- [39] J. L. Zhang, C. M. Wang, C. Y. Guo, X. D. Zhu, Y. Zhang, J. Y. Yang, Y. Q. Wang, Z. Qu, L. Pi, H. Z. Lu, and M. L. Tian, Anomalous Thermoelectric Effects of  $\text{ZrTe}_5$  in and beyond the Quantum Limit, *Phys. Rev. Lett.* **123**, 196602 (2019).
- [40] E. Martino, I. Crassee, G. Eguchi, D. Santos-Cottin, R. D. Zhong, G. D. Gu, H. Berger, Z. Rukelj, M. Orlita, C. C. Homes, and A. Akrap, Two-Dimensional Conical Dispersion in  $\text{ZrTe}_5$  Evidenced by Optical Spectroscopy, *Phys. Rev. Lett.* **122**, 217402 (2019).
- [41] Y. Jiang, J. Wang, T. Zhao, Z. L. Dun, Q. Huang, X. S. Wu, M. Mourigal, H. D. Zhou, W. Pan, M. Ozerov, D. Smirnov, and Z. Jiang, Unraveling the Topological Phase of  $\text{ZrTe}_5$  via Magnetoinfrared Spectroscopy, *Phys. Rev. Lett.* **125**, 046403 (2020).
- [42] W. Wu, Z. Shi, Y. Du, Y. Wang, F. Qin, X. Meng, B. Liu, Y. Ma, Z. Yan, M. Ozerov, C. Zhang, H.-Z. Lu, J. Chu, and X. Yuan, Topological Lifshitz transition and one-dimensional Weyl mode in  $\text{HfTe}_5$ , *Nat. Mater.* **22**, 84 (2023).

- [43] L. Fu, C. L. Kane, and E. J. Mele, Topological Insulators in Three Dimensions, *Phys. Rev. Lett.* **98**, 106803 (2007).
- [44] L. Fu and C. L. Kane, Topological insulators with inversion symmetry, *Phys. Rev. B* **76**, 045302 (2007).
- [45] B. Yan, L. Muechler, and C. Felser, Prediction of weak topological insulators in layered semiconductors, *Phys. Rev. Lett.* **109**, 116406 (2012).
- [46] See Supplemental Material at [xxx] for detailed calculations, which includes Refs.[33-45,47-49,53,54,67-70].
- [47] P. Štředa, Theory of quantised Hall conductivity in two dimensions, *J. Phys. C* **15**, L717 (1982).
- [48] X.-L. Qi and S.-C. Zhang, Topological insulators and superconductors, *Rev. Mod. Phys.* **83**, 1057 (2011).
- [49] H.-Z. Lu, W.-Y. Shan, W. Yao, Q. Niu, and S.-Q. Shen, Massive dirac fermions and spin physics in an ultrathin film of topological insulator, *Phys. Rev. B* **81**, 115407 (2010).
- [50] A. A. Varlamov and A. V. Pantsulaya, Anomalous kinetic properties of metals near the Lifshitz topological transition, *Zh. Eksp. Teor. Fiz.* **62**, 1263 (1985).
- [51] V. E. A.A. Varlamov and A. Pantsulaya, Kinetic properties of metals near electronic topological transitions (2 1/2-order transitions), *Adv. Phys.* **38**, 469 (1989).
- [52] Y. Blanter, M. Kaganov, A. Pantsulaya, and A. Varlamov, The theory of electronic topological transitions, *Phys. Rep.* **245**, 159 (1994).
- [53] G. D. Mahan, *Many Particle Physics, Third Edition* (Plenum, New York, 2000).
- [54] C.-L. Zhang, C. M. Wang, Z. Yuan, X. Xu, G. Wang, C.-C. Lee, L. Pi, C. Xi, H. Lin, N. Harrison, H.-Z. Lu, J. Zhang, and S. Jia, Non-saturating quantum magnetization in Weyl semimetal TaAs, *Nat. Commun.* **10**, 1028 (2019).
- [55] D. Xiao, Y. Yao, Z. Fang, and Q. Niu, Berry-phase effect in anomalous thermoelectric transport, *Phys. Rev. Lett.* **97**, 026603 (2006).
- [56] A. Gourgout, M. Leroux, J. L. Smirr, M. Massoudzadegan, R. P. Lobo, D. Vignolles, C. Proust, H. Berger, Q. Li, G. Gu, C. C. Homes, A. Akrap, and B. Fauqué, Magnetic freeze-out and anomalous Hall effect in ZrTe<sub>5</sub>, *npj Quantum Mater.* **7**, 71 (2022).
- [57] P.-J. Shih, C.-H. Yang, P.-C. Liao, W.-C. Lin, F.-H. Chen, J.-C. Chen, L. Cao, C. Chuang, and C.-T. Liang, Unveiling the phases of bulk ZrTe<sub>5</sub> through magnetotransport phenomena, *Nanotechnology* **36**, 095204 (2025).
- [58] Y. Zhang, Q. Li, P. Zhao, Y. Qian, Y. Lv, Y. Chen, Q. Niu, H. Lu, J. Zhang, and M. Tian, Observation of Giant Nernst plateau in ideal 1D Weyl Phase, [arXiv:2410.11154](https://arxiv.org/abs/2410.11154).
- [59] T. Liang, J. Lin, Q. Gibson, S. Kushwaha, M. Liu, W. Wang, H. Xiong, J. A. Sobota, M. Hashimoto, P. S. Kirchmann, Z. X. Shen, R. J. Cava, and N. P. Ong, Anomalous Hall effect in ZrTe<sub>5</sub>, *Nat. Phys.* **14**, 451 (2018).
- [60] F. Tang, Y. Ren, P. Wang, R. Zhong, J. Schneeloch, S. A. Yang, K. Yang, P. A. Lee, G. Gu, Z. Qiao, and L. Zhang, Three-dimensional quantum Hall effect and metal-insulator transition in ZrTe<sub>5</sub>, *Nature* **569**, 537 (2019).
- [61] H. Wang, H. Liu, Y. Li, Y. Liu, J. Wang, J. Liu, J. Y. Dai, Y. Wang, L. Li, J. Yan, D. Mandrus, X. C. Xie, and J. Wang, Discovery of log-periodic oscillations in ultraquantum topological materials, *Sci. Adv.* **4**, aau5096 (2018).
- [62] P. Shahi, D. J. Singh, J. P. Sun, L. X. Zhao, G. F. Chen, Y. Y. Lv, J. Li, J.-Q. Yan, D. G. Mandrus, and J.-G. Cheng, Bipolar conduction as the possible origin of the electronic transition in pentatellurides: Metallic vs semiconducting behavior, *Phys. Rev. X* **8**, 021055 (2018).
- [63] E. Gornik, R. Lassnig, G. Strasser, H. L. Störmer, A. C. Gossard, and W. Wiegmann, Specific Heat of Two-Dimensional Electrons in GaAs-GaAlAs Multilayers, *Phys. Rev. Lett.* **54**, 1820 (1985).
- [64] T. P. Smith, B. B. Goldberg, P. J. Stiles, and M. Heiblum, Direct measurement of the density of states of a two-dimensional electron gas, *Phys. Rev. B* **32**, 2696 (1985).
- [65] R. Ashoori and R. Silsbee, The Landau level density of states as a function of Fermi energy in the two dimensional electron gas, *Solid State Commun.* **81**, 821 (1992).
- [66] C. Wang, Thermodynamically Induced Transport Anomaly in Dilute Metals ZrTe<sub>5</sub> and HfTe<sub>5</sub>, *Phys. Rev. Lett.* **126**, 126601 (2021).
- [67] A. A. Abrikosov, Quantum magnetoresistance, *Phys. Rev. B* **58**, 2788 (1998).
- [68] H.-Z. Lu, S.-B. Zhang, and S.-Q. Shen, High-field magnetoconductivity of topological semimetals with short-range potential, *Phys. Rev. B* **92**, 045203 (2015).
- [69] H.-Z. Lu and S.-Q. Shen, Weak antilocalization and localization in disordered and interacting Weyl semimetals, *Phys. Rev. B* **92**, 035203 (2015).
- [70] S.-B. Zhang, H.-Z. Lu, and S.-Q. Shen, Linear magnetoconductivity in an intrinsic topological Weyl semimetal, *New J. Phys.* **18**, 053039 (2016).